

RESEARCH LETTER

10.1002/2015GL065530

Key Points:

- Satellite and OOI Pioneer Array data show ring water intruding onto the shelf
- The intrusions extend southwestward along the shelf edge over large distances
- Vortex squashing of the ring flow by the rising seafloor drives the intrusion

Correspondence to:

W. G. Zhang,
wzhang@whoi.edu

Citation:

Zhang, W. G., and G. G. Gawarkiewicz (2015), Dynamics of the direct intrusion of Gulf Stream ring water onto the Mid-Atlantic Bight shelf, *Geophys. Res. Lett.*, 42, 7687–7695, doi:10.1002/2015GL065530.

Received 24 JUL 2015

Accepted 20 AUG 2015

Accepted article online 25 AUG 2015

Published online 30 SEP 2015

Dynamics of the direct intrusion of Gulf Stream ring water onto the Mid-Atlantic Bight shelf

Weifeng G. Zhang¹ and Glen G. Gawarkiewicz²
¹Applied Ocean Physics and Engineering Department, Woods Hole Oceanographic Institution, Woods Hole, Massachusetts, USA, ²Physical Oceanography Department, Woods Hole Oceanographic Institution, Woods Hole, Massachusetts, USA

Abstract Onshore intrusions of offshore waters onto the Mid-Atlantic Bight shelf can greatly affect shelf circulation, biogeochemistry, and fisheries. Previous studies have concentrated on onshore intrusions of slope water. Here we present a direct intrusion of Gulf Stream warm-core ring water onto the shelf representing a previously unknown exchange process at the shelfbreak. Impingement of warm-core rings at the shelfbreak generates along-isobath intrusions that grow like Pinocchio's nose, extending hundreds of kilometers to the southwest. By combining satellite and Ocean Observatory Initiative Pioneer Array data and idealized numerical simulations, we discover that the intrusion results from topographically induced vorticity variation of the ring water, rather than from entrainment of the shelfbreak frontal jet. This intrusion of the Gulf Stream ring water has important biogeochemical implications and could facilitate migration of marine species across the shelfbreak barrier and transport low-nutrient surface Gulf Stream ring water to the otherwise productive shelfbreak region.

1. Introduction

Because of its high-latitude origin [Chapman and Beardsley, 1989], water on the Mid-Atlantic Bight (MAB) shelf is generally colder, fresher, and less dense than the slope waters [Linder and Gawarkiewicz, 1998], and its biogeochemical properties also differ dramatically from the offshore waters [Wang et al., 2013]. The cross-shelf density gradient is large at the shelfbreak front, driving an equatorward geostrophic shelfbreak jet [Houghton et al., 2006]. Onshore intrusions of the offshore waters affect shelf circulation and biogeochemistry [Gawarkiewicz et al., 1996; Lentz, 2003]; the onshore salt flux induced by shelfbreak exchange is a key for maintaining along-shelf density homogeneity [Lentz, 2010]. Shelfbreak exchange processes include cross-frontal eddy transport [Gawarkiewicz et al., 2004], midcolumn saline intrusions [Lentz, 2003], wind-driven near-surface flows [Gawarkiewicz et al., 1996], and topographically influenced bottom flows [Allen and Durrieu de Madron, 2009].

Anticyclonic warm-core rings (WCRs) of >1000 m deep developing from Gulf Stream meanders (Figure 1a) are common features over the continental slope [e.g., Evans et al., 1985; Wei and Wang, 2009]. Shallower ringlets [Kennelly et al., 1985] and limbs (Figure 1a) of ~100 m deep may develop on the ring periphery. A WCR impinging on the continental slope can induce substantial cross-shelf water exchange. It can pull the shelf water offshore, generating a shelf water streamer [e.g., Cenedese et al., 2013; Ryan et al., 2001]. Presumably, ring water can also move onshore resupplying the shelf and affecting shelf biology [Cowen et al., 1993; Flierl and Wroblewski, 1985]. However, the physical mechanism of this onshore motion is unknown. This paper describes a type of direct onshore intrusion of the Gulf Stream ring water previously unknown and presents the underlying mechanism.

2. Observations

Satellite sea surface temperature (SST) in winter and spring in the presence of impinging WCRs sometimes show elongated warm water intrusions growing along the MAB shelfbreak from the ring-shelf contact region reaching hundreds of kilometers to the west/southwest. For instance, shelfbreak-trapped intrusions were present at the southern MAB in March 1982 [Evans et al., 1985], south of Georges Bank in June 1997 [Lee and Brink, 2010] and May 1999 [Brown et al., 2005], and offshore of New Jersey in April 2006 (Figure 1e). Because the intrusion resembles the expansion of Pinocchio's nose (see below), we hereafter refer to it as Pinocchio's nose intrusion, PNI, or nose.

©2015. The Authors.

This is an open access article under the terms of the Creative Commons Attribution-NonCommercial-NoDerivs License, which permits use and distribution in any medium, provided the original work is properly cited, the use is non-commercial and no modifications or adaptations are made.

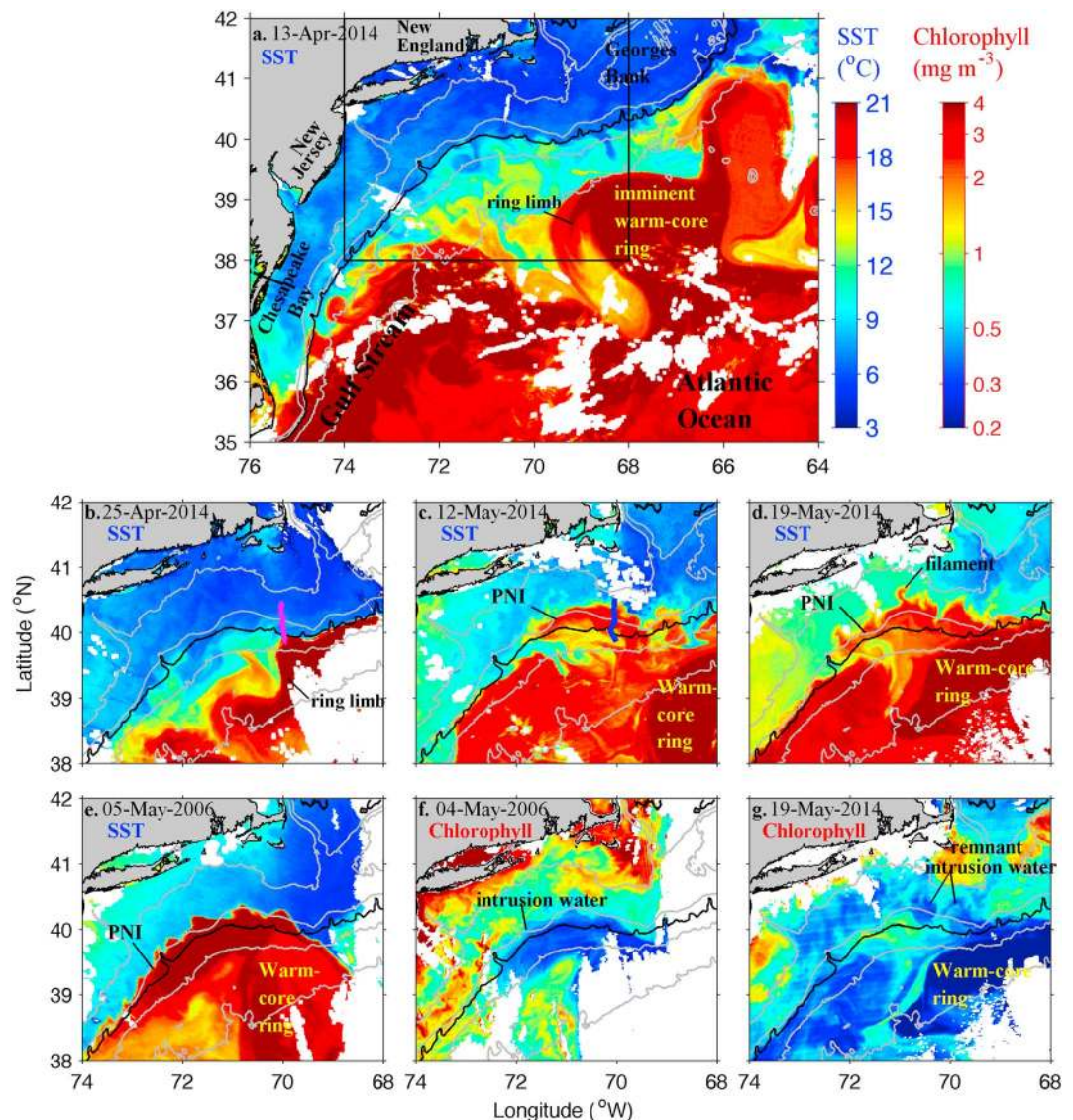


Figure 1. Sea surface (a–e) temperature and (f, g) chlorophyll. The black curve is the 200 m isobath; the gray curves are 50, 100, 2000, and 3000 m isobaths. The magenta and blue lines in Figures 1b and 1c show glider tracks on 25–28 April and 8–13 May 2014, respectively. White patches are missing data due to cloud cover.

Sporadically available MAB SST images in the winter and spring seasons of 2007–2014 show approximately five PNI-like events (e.g., Figures 1b–1d). These PNI features appear similar to warm filaments in the Southern Atlantic Bight (SAB) shelf developed from the Gulf Stream [e.g., Lee *et al.*, 1981]. Contrary to SAB filaments moving northward with the Gulf Stream, the MAB PNIs move equatorward opposing the motion of their sources immediately offshore—eastward flow on the onshore edge of the ring. Without subsurface information to define the vertical structure, SST does not reveal the PNI formation mechanism. The first glider mission of the National Science Foundation Ocean Observatories Initiative (OOI) Pioneer Array over April–June 2014 conveniently sampled a PNI and showed subsurface conditions before and after its formation (Figure 2). The vertical structure, together with SST, provides an unprecedented opportunity to study PNI dynamics.

The 2014 PNI was formed after a ring limb reached the shelfbreak at 70°W (Figures 1b–1d). The nose tip moved westward along the 100 m isobath with a speed of $\sim 0.15 \text{ ms}^{-1}$, covering 200 km in 15 days. During 25–28 April, as the limb reached the shelfbreak, the glider cross section shows the shelfbreak front and the

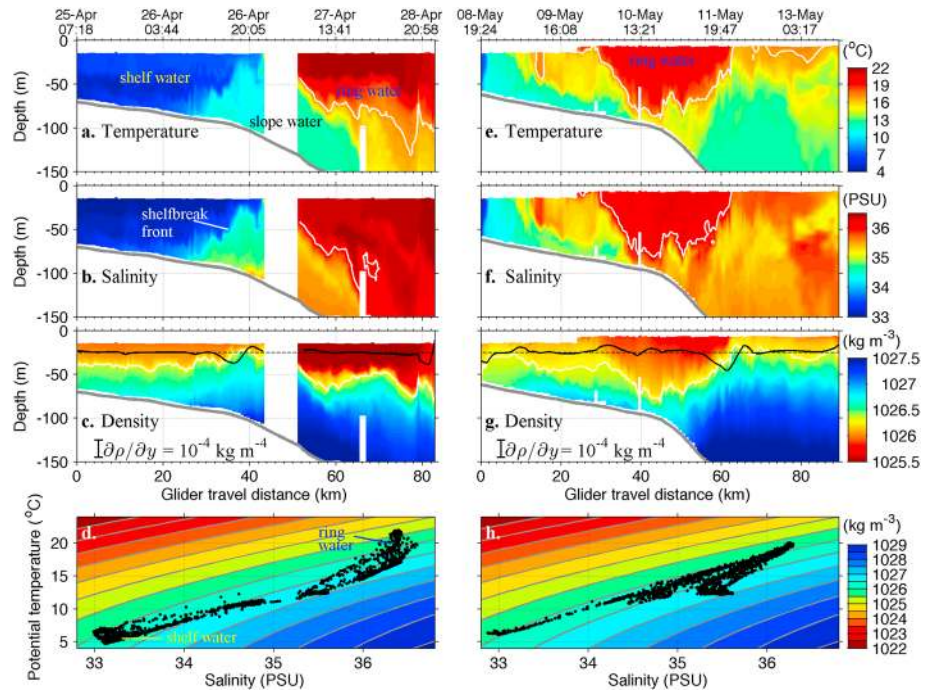


Figure 2. Glider measurements on (a–c) 25–28 April and (e–g) 8–13 May 2014 and temperature/salinity diagrams of the data in (d) Figures 2a and 2b and (h) Figures 2e and 2f averaged in 5 m vertical bins. White lines are 17°C isothermal, 36 isohaline, and 1026.3 kg m^{−3} isopycnal. Black solid lines indicate cross-shelf density gradient, $\partial\rho/\partial y$, at $z = -25$ m (positive y points shoreward). White patches in Figures 2a–2c and 2e–2g represent missing data.

warm and saline ring water (Figures 2a–2c). Surface density of the ring and shelf waters are $\rho_r \approx 1025.3$ kg m^{−3} and $\rho_{sh} \approx 1025.9$ kg m^{−3}, respectively, and surface density of the slope water is $\rho_{sl} \approx 1026.6$ kg m^{−3}, as measured by another glider 40 km to the west (not shown). Therefore, $\rho_r < \rho_{sh} < \rho_{sl}$. The temperature/salinity diagram (Figure 2d) reveals that the dramatic temperature difference between the shelf and ring waters, 5°C versus 22°C, overcame the salinity influence on density and caused $\rho_r < \rho_{sh}$.

During 8–13 May 2014 the PNI formed, and the glider-measured vertical structure shows the nose, ~80 m thick, extending close to the seafloor and sandwiched by diluted shelf water onshore and slope water offshore (Figures 2e–2g). There was no shelfbreak front beneath the nose, and the intrusion was thus not a surface feature carried along by an underlying shelfbreak frontal jet. At this time, $\partial\rho/\partial y > 0$ (< 0) at the onshore (offshore) edge of the nose and, because $\rho_r < \rho_{sh} < \rho_{sl}$, $|\partial\rho/\partial y|$ was greater at the offshore edge than at the onshore edge (Figure 2g). Here we define y as positive in the shoreward direction, x positive northeastward along shelf, and z positive upward. Assuming thermal-wind balance, $\partial u/\partial z = g(\partial\rho/\partial y)/(\rho_0 f)$, $|\partial u/\partial z|$ was greater at the offshore edge of the nose than at the onshore edge. Here u is the along-shelf velocity, g the gravitational acceleration, f the Coriolis parameter, and $\rho_0 = 1025$ kg m^{−3} the reference density. Assuming the whole cross-section synoptic and zero velocity below $z = -150$ m and on the shelf bottom, we obtain the maximum near-surface u of 0.3 m s^{−1} and -0.6 m s^{−1} at the onshore and offshore nose edges, respectively. The along-shelf velocity averaged over the nose cross-section $u_a \approx -0.1$ m s^{−1}. Thus, the asymmetrical nose edge $|\partial\rho/\partial y|$ resulting from density differences between the three water masses likely causes a westward net transport of the ring water and contributes to the PNI.

Using the maximum speed of $|u| \approx 0.6$ m s^{−1} and the nose width of $W = 20$ –40 km gives the Rossby number of the intrusion flow, $Ro = |u|/fW = 0.2 - 0.3 \sim O(1)$, indicating the lowest-order importance of momentum advection. The observed mean buoyancy frequency at the shelfbreak is $N \approx 0.01$ s^{−1}. Bottom slope at the shelfbreak is $\alpha \approx 0.01$. Thus, the normalized shelfbreak bottom slope [Trowbridge and Lentz, 1991], $S = \alpha N/f \approx 1 \sim O(1)$, indicating strong topographic influence on the intrusion flow. This is consistent with the observed nose expansion being primarily along isobath.

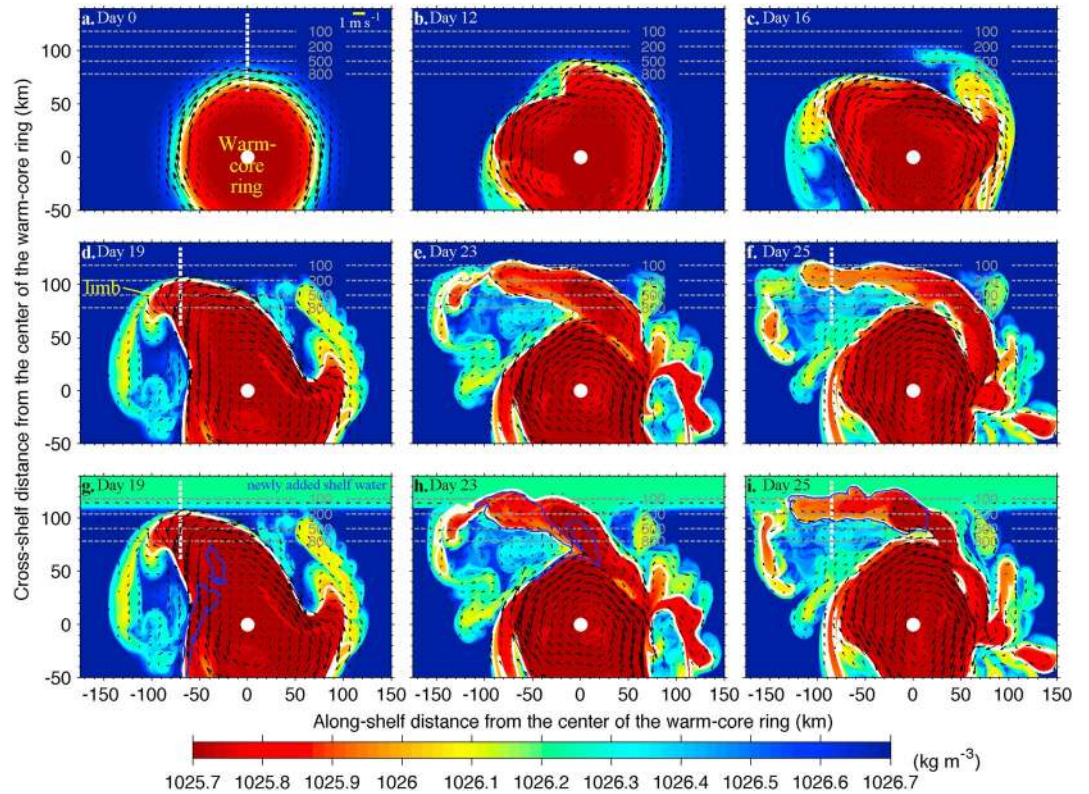


Figure 3. Surface density (color) and velocity (vectors at every 20 grid points) from (a–f) Simulation 1 and (g–i) Simulation 2. White solid lines are contours of 75% ring water concentration. White dashed lines indicate locations of the cross sections in Figure 4. Blue lines in Figures 3g–3i depict the source regions of the ring water that occupies the nose on Day 25.

About 15 days after the intrusion started, SST images show deformation of the onshore edge of the nose with warm water intruding further shoreward in cross-isobath filaments ~5 km wide (Figure 1d). Presumably, frontal instability or shelf eddy entrainment caused this cross-isobath motion.

3. Model Analysis

3.1. Configuration

The Regional Ocean Modeling System [Shchepetkin and McWilliams, 2008] is used to solve nonlinear momentum and density equations in a rectangle domain of 2010.5 km (in x) \times 479 km (in y) with a horizontal resolution of 500 m and 60 vertical layers. The model bathymetry is uniform in the x (along-shelf) direction. Its cross-shelf variation is an idealization of the MAB shelfbreak bathymetry [Zhang and Gawarkiewicz, 2015]: it starts from 10 m deep northern coastal wall, deepens southward with a slope of $\alpha \approx 0.5 \times 10^{-3}$ to the 100 m isobath, 140 km south of the northern wall, and then transitions to a hyperbolic tangent-shaped continental slope with a maximum depth of 1005 m.

Model initial density consists of an idealized WCR residing in the slope water of horizontally uniform and vertically varying density from an observed MAB density profile with surface density $\rho_{sl} = 1026.7 \text{ kg m}^{-3}$. The circular WCR has density anomaly relative to the slope water (Figure 3a)

$$\Delta\rho_r(x, y, z) = \frac{1}{2} \left[1 - \tanh\left(\frac{r - r_c}{r_b}\right) \right] \exp\left[-\frac{z^2}{h_r^2}\right] \Delta\rho_0. \quad (1)$$

Here $\Delta\rho_0 = -1 \text{ kg m}^{-3}$ is the surface density anomaly at the ring center, (x_0, y_0) , 121 km south of the 100 m isobath; $r = [(x - x_0)^2 + (y - y_0)^2]^{1/2}$; $r_c = 75 \text{ km}$ is the ring radius; $r_b = 15 \text{ km}$; $h_r = 425 \text{ m}$. The surface density of the ring water $\rho_r = \rho_{sl} + \Delta\rho_0 = 1025.7 \text{ kg m}^{-3}$, and the difference of $|\Delta\rho_0| = 1 \text{ kg m}^{-3}$ is chosen to resemble the observed density difference. Geostrophically balanced horizontal velocity (maximum speed of

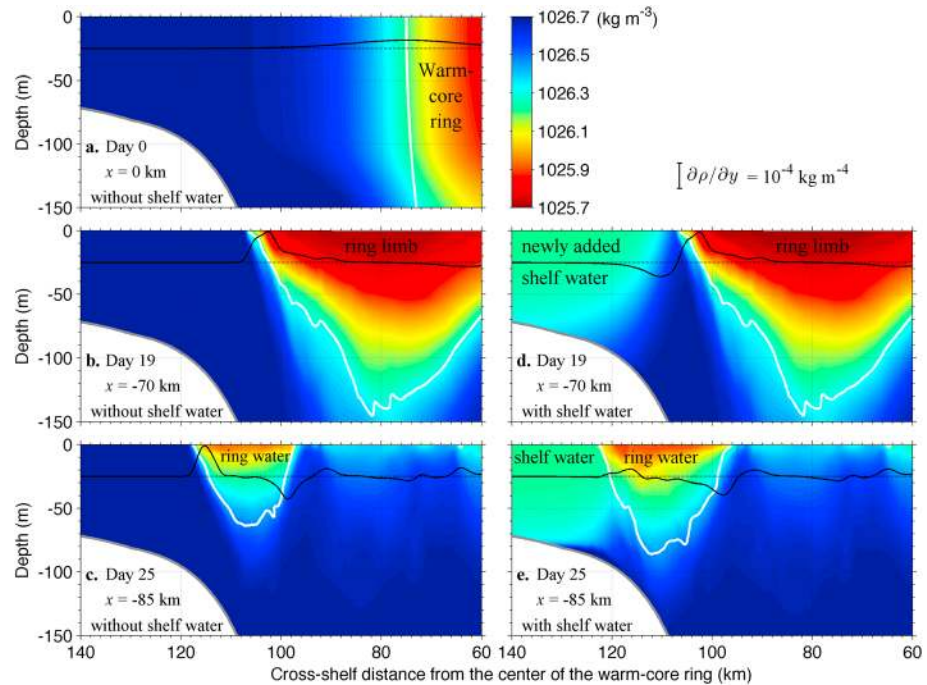


Figure 4. Density cross sections along the white dashed lines in Figures (a) 3a, (b) 3d, (c) 3f, (d) 3g, and (e) 3i, respectively. Black solid lines indicate $\partial\rho/\partial y$ at $z = -25$ m. White lines are contours of 75% ring water concentration.

1.27 m s^{-1}) and sea level tilt are added to the model initial conditions. To facilitate the perturbation growth, Gaussian random velocity perturbation with zero mean and standard deviation of 0.02 m s^{-1} is added to the ring.

The shelf water is characterized by negative, along-shelf uniform density anomaly (Figure 3g), which generates a shelfbreak front with isopycnals rising from the ocean floor offshore (Figure 4d). The shelf water surface density $\rho_{\text{sh}} = 1026.2 \text{ kg m}^{-3}$, satisfying $\rho_r < \rho_{\text{sh}} < \rho_{\text{sl}}$. The density distribution resembles a typical wintertime MAB shelfbreak frontal structure [Fratantoni *et al.*, 2001; Gawarkiewicz *et al.*, 2001; Zhang and Gawarkiewicz, 2015].

Along-shelf periodic boundary conditions are applied in all simulations. Horizontal viscosity and diffusivity are 0 in the 289 km inshore study area and increase linearly in a 190 km wide (in y) sponge layer reaching $100 \text{ m}^2 \text{ s}^{-1}$ at the southern boundary. A general length scale vertical turbulence closure k - kl scheme [Warner *et al.*, 2005] and quadratic bottom drag with coefficient of 0.003 are used. There is no surface forcing. The model includes a ring water concentration passive tracer with initial value of 1 in the WCR and 0 elsewhere. Transport of the passive tracer across the 200 m isobath is computed as the intrusion volume transport, Q_v .

Here we focus on the formation of the intrusion within the first 25 days (~ 32 inertial periods) of the simulations and neglect the subsequent WCR evolution. We compare two f plane ($f = f_0 = 9.37 \times 10^{-5} \text{ s}^{-1}$) simulations of the WCR impingement with and without the shelfbreak front. Simulation 1 is initialized with only slope and ring waters. The slope water extends horizontally onto the shelf with no $\partial\rho/\partial y$ at the shelfbreak. Simulation 2 contains shelf, slope, and ring waters. Its initial conditions are obtained by first extracting Simulation 1 fields at Day 19, just before a limb reaches the shelfbreak (Figure 3d), and then adding the shelf density anomaly and associated shelfbreak jet (Figures 3g and 4d). We do not start Simulation 2 from an undisturbed WCR because early-stage interaction between the ring and shelfbreak front would affect the growth of the ring instability in the slope sea and result in a slightly different limb shape. This would then affect details of the PNI although not the fundamental pattern. The hybrid initialization is chosen to avoid the ambiguity between this early-stage influence and that of the asymmetrical nose edge $|\partial\rho/\partial y|$. Differences between Simulation 1 and Simulation 2 reveal only the influence of the asymmetrical $|\partial\rho/\partial y|$ on the intrusion flow.

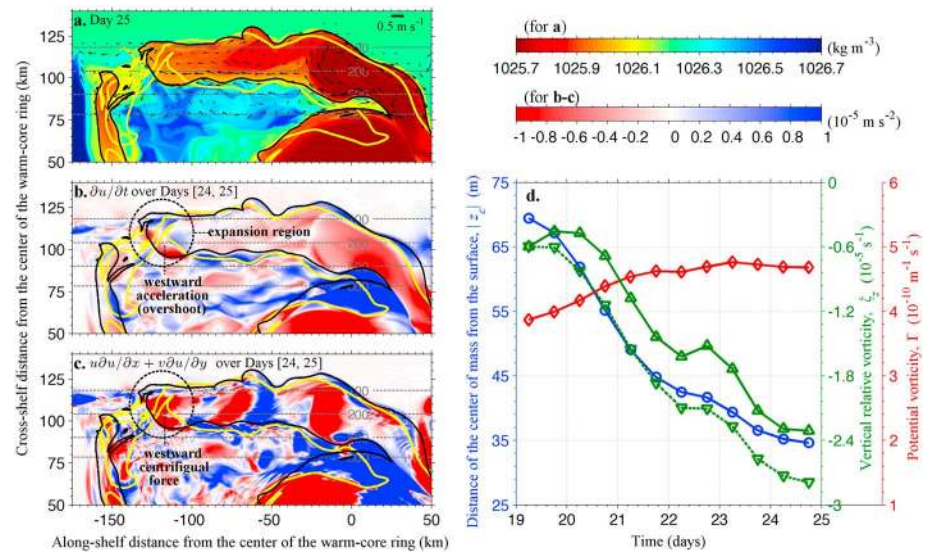


Figure 5. Surface (a) density (color) and velocity (vectors at every 15 grid points) on Day 25 and averaged (b) acceleration and (c) horizontal momentum advection terms over Days 24–25 from Simulation 2. Yellow and black lines are contours of 75% ring water concentration on Days 24 and 25, respectively. (d) Variations of $|z_c|$ (blue), Π (red), ζ_z (solid green), and ζ_{z0} (dashed green) of the ring water before its occupation of the nose on Day 25.

3.2. Results

In Simulation 1, WCR baroclinic instability generates meanders growing into limbs propagating clockwise along the ring periphery (Figures 3a–3d). The limbs extend to a depth of ~ 150 m (Figure 4b), consistent with the vertical scale of observed ringlets [Kennelly *et al.*, 1985]. After a northwest pointing limb reaches the shelf-break, it develops into a PNI of 20–40 km wide and ~ 60 m thick (Figures 3e and 3f and 4c) expanding westward along the shelfbreak with a speed of ~ 0.14 m s⁻¹, qualitatively resembling the observed PNI. The mean onshore volume transport $Q_v \approx 0.15$ sverdrup (Sv). The PNI occurring in this simulation with no shelfbreak front confirms that it does not result from entrainment of the shelfbreak frontal jet. Without the shelf water, $|\partial p / \partial y|$ at the onshore and offshore nose edges are roughly the same in this simulation (Figure 4c), indicating that the asymmetrical nose edge $|\partial p / \partial y|$ is not a necessary condition for the PNI to occur. The model shows anticyclonic flow within the nose with the maximum speed of $|u|_{\max} \approx 0.75$ m s⁻¹. Using $|u|_{\max}$, we obtain $Ro = 0.2$ – 0.4 , and the modeled nose has $S \approx 1$, consistent with observations.

The basic intrusion pattern in Simulation 2 is the same as that in Simulation 1 with also $Ro = 0.2$ – 0.4 and $S \approx 1$, but the addition of the shelf water creates asymmetrical $|\partial p / \partial y|$ with greater $|\partial p / \partial y|$ and then $|u|$ at the offshore edge (Figures 4e and 5a). In Simulation 2 the nose is wider and thicker (Figure 4e) and propagates westward slightly faster (Figure 3i), resulting in a greater $Q_v \approx 0.33$ Sv. This change suggests that through supplying ring water toward the nose tip, the asymmetrical nose edge $|\partial p / \partial y|$ in the presence of the shelf water greatly enhances the PNI.

The Simulation 2 along-shelf momentum balance shows that horizontal momentum advection, i.e., the westward centrifugal force, at the nose tip causes an overshoot of the initially along-isobath flow at the abrupt turning point. As the ring water continuously flows into the nose tip, this overshoot drives the persistent along-shelf expansion (Figures 5a–5c). This effect of the excessive momentum advection is consistent with $Ro \sim O(1)$ in the modeled PNI and confirmed by a simulation the same as Simulation 2 but without momentum advection. In this third simulation, the PNI does not form and the ring water turns sharply to the east at the 200 m isobath (not shown).

Vorticity analysis of the intrusion water in Simulation 2 reveals that the topographic forcing exerted on the approaching ring limb initiates the intrusion. Here we identify source regions of the ring water prior to its occupation of the nose on Day 25 (Figures 3g–3i) using an adjoint tracer model [Zhang *et al.*, 2010]. The adjoint simulation starts from the nose volume on Day 25 (blue line in Figure 3i) and simulates the backward

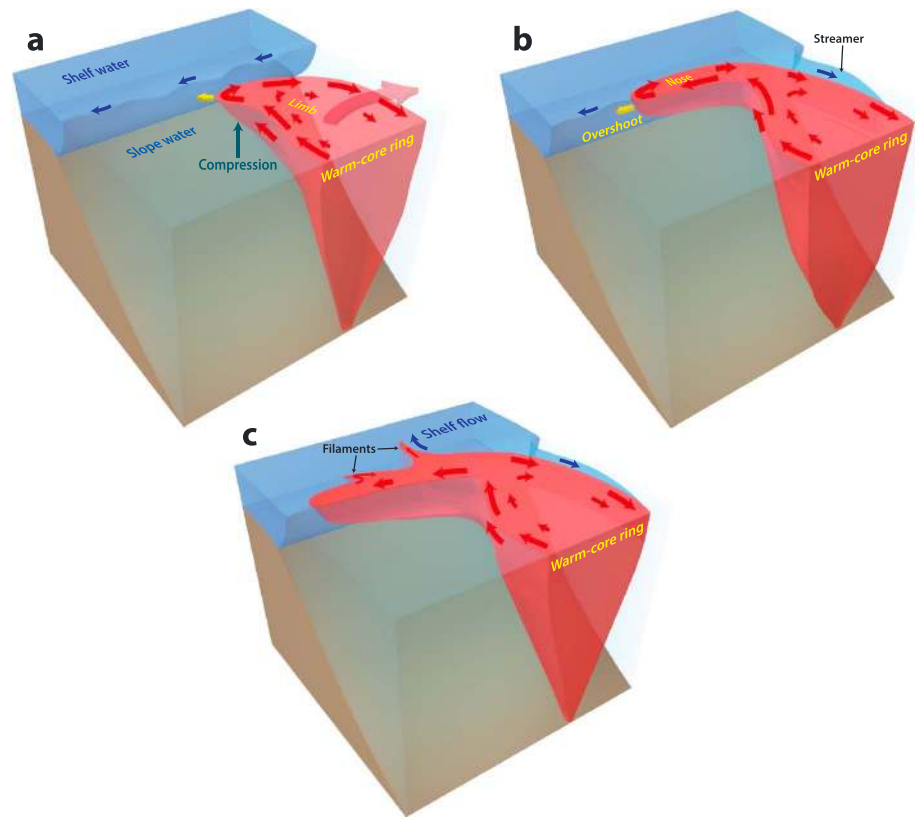


Figure 6. Schematics depicting the evolution of the intrusion process.

tracer advection and diffusion. Note that because the flow is faster than the limb motion, the source regions locate upstream of the limb on Day 19 (Figure 3g).

Evolution of the source volume (Figure 5d) indicates that as the water flows into the nose, its center of mass rises from $z_c = -67$ m on Day 19 to -35 m on Day 25. During this process, magnitude of the vertical relative vorticity, $\zeta_z = -\partial u/\partial y + \partial v/\partial x$, averaged over the source volume increases by 360%, while the volume-averaged potential vorticity, $\Pi = [-\zeta_x \partial \rho/\partial x - \zeta_y \partial \rho/\partial y - (\zeta_z + f) \partial \rho/\partial z]/\rho_0$ (the last term dominant), increases by only 20%. Here ζ_x and ζ_y are relative vorticity in the x and y directions, respectively. The dramatic variation of ζ_z is largely consistent with the scaled variation of relative vorticity, $\zeta_{z0} = 2|z_c|[\Pi\rho_0/\Delta\rho - f]$, of a water volume of homogeneous density anomaly $\Delta\rho = 1 \text{ kg m}^{-3}$ responding to the changes in thickness ($2|z_c|$) and Π (Figure 5d; assuming $\zeta_{z0} = \zeta_z$ on Day 19). This suggests that as Π is largely conserved, topographic squeezing enhances the anticyclonic flow within the limb, strengthens the outward centrifugal force, and initiates the intrusion.

Overall, interaction of the shelfbreak topography with flow vorticity drives the PNI (Figure 6). As the north-west pointing ring limb approaches the shelfbreak, the rising seafloor squeezes it vertically and intensifies its anticyclonic flow. The strengthened centrifugal force pushes the ring water outward. Strong topographic constraints at the shelfbreak inhibit the cross-isobath flow and force the expansion to follow isobaths creating the PNI. Flow overshoot at the nose tip expands it further along the shelfbreak. The asymmetrical cross-shelf density gradients at the opposite nose edges drive a westward transport supplying more ring water toward the nose tip and enhancing its expansion. The elongated nose shape creates a wide interface between the ring and shelf waters and facilitates the subsequent ring water onshore penetration through shelf processes, as indicated by the observed cross-isobath warm filaments (Figure 1d). Due to lack of shelf circulation and external forcing, the models do not produce these filaments.

Sensitivity simulations show that the intrusion strength is sensitive to the water density, position, and motion of the WCR: Q_v increases with density anomaly, horizontal proximity to the shelf edge and

cross-shelf motion of the ring. A simulation initialized with three water masses but halved ring water density anomaly ($\rho_r = \rho_{sh} = \rho_{sl} - 0.5 \text{ kg m}^{-3}$) gives $Q_v \approx 0.033 \text{ Sv}$, much smaller than 0.33 Sv in Simulation 2. A simulation with a WCR 5 km closer to the shelfbreak than Simulation 2 gives $Q_v \approx 0.38 \text{ Sv}$. A simulation with a meridionally varying Coriolis parameter $f = f_0 + \beta y$ ($\beta = 1.75 \times 10^{-11} \text{ m}^{-1} \text{ s}^{-1}$) shows a weaker intrusion of $Q_v \approx 0.16 \text{ Sv}$, as a result of the WCR moving southwestward away from the shelfbreak due to nonlinear Rossby wave propagation [Early *et al.*, 2011]. Representing a westward propagating WCR impinging at the north-south oriented southern MAB shelfbreak, a simulation with zonally varying $f = f_0 + \beta x$ ($\beta = 1.75 \times 10^{-11} \text{ m}^{-1} \text{ s}^{-1}$) gives $Q_v \approx 0.46 \text{ Sv}$. Further analysis is needed to rationalize these parameter dependences.

4. Implications

This direct intrusion of the Gulf Stream ring water onto the MAB shelf can contribute significantly to the shelf mass and heat balance. Assuming the nose on 12 May 2014 as a triangular prism with a surface base of $200 \times 35 \text{ km}^2$ and a height of 80 m, the mean onshore volume transport $Q_v \approx 0.22 \text{ Sv}$. It is significant compared to the mean shelfbreak jet transport of $0.2\text{--}0.4 \text{ Sv}$ [Fratantoni *et al.*, 2001] and the offshore transport of $\sim 0.28 \text{ Sv}$ in the 2006 shelf water streamer [Chen *et al.*, 2014]. Applying a temperature difference between the shelf and ring waters of $\Delta T = 10^\circ\text{C}$, the mean onshore heat transport of the 2014 intrusion is $Q_t = \rho_0 C_p Q_v \Delta T \approx 9.4 \times 10^{12} \text{ W}$, $>50\%$ of the maximum monthly mean surface upward heat transport over the entire MAB shelf ($\sim 100 \times 800 \text{ km}^2$) [Lentz, 2010]. Here $C_p = 4190 \text{ J}(\text{kg } ^\circ\text{C})^{-1}$ is seawater heat capacity.

The direct intrusion has important biogeochemical implications. It can break the shelfbreak transport barrier and facilitate the migration of marine species onto the MAB shelf [Hare *et al.*, 2002]. For instance, it may contribute to the fast transport of bluefish [Hare and Cowen, 1996] and eel [Rypina *et al.*, 2014] larvae from their spawning grounds in the far south to MAB nursery habitats. Meanwhile, the intrusion may suppress shelfbreak biological productivity by importing low-nutrient Gulf Stream water [Brown *et al.*, 1985] (Figures 1f and 1g) to the otherwise productive shelfbreak region [Ryan *et al.*, 1999; Zhang *et al.*, 2013].

Acknowledgments

Satellite SST data were obtained from the Rutgers University Coastal Ocean Observation Laboratory through the Mid-Atlantic Regional Association Coastal Ocean Observing System data server (<http://tds.maracoos.org/thredds/SST.html>). Satellite chlorophyll data were retrieved from the Ocean Color online data server (<http://ocean-color.gsfc.nasa.gov/>). This material is partially based upon precommissioned glider data (<https://confluence.ocean-observatories.org/display/data/Pioneer+Array>) from the Ocean Observatories Initiative (OOI), a Program funded by the National Science Foundation. The processed data sets presented in this work are available upon request at wzhang@whoi.edu. The authors are supported by the National Science Foundation through grant OCE-1129125. The authors thank Kenneth Brink, Ke Chen, Timothy Duda, Paula Fratantoni, Rocky Geyer, Gareth Lawson, Steven Lentz, Dennis McGillicuddy, Albert Plueddemann, and John Trowbridge for helpful discussions and comments on an early draft.

The Editor thanks James Manning and an anonymous reviewer for their assistance in evaluating this paper.

References

- Allen, S. E., and X. Durrieu de Madron (2009), A review of the role of submarine canyons in deep-ocean exchange with the shelf, *Ocean Sci.*, 5(4), 607–620, doi:10.5194/os-5-607-2009.
- Brown, H., S. M. Bollens, L. P. Madin, and E. F. Horgan (2005), Effects of warm water intrusions on populations of macrozooplankton on Georges Banks, Northwest Atlantic, *Cont. Shelf Res.*, 25, 143–156.
- Brown, O. B., R. H. Evans, J. W. Brown, H. R. Gordon, R. C. Smith, and K. S. Baker (1985), Phytoplankton blooming off the U.S. east coast: A satellite description, *Science*, 229(4709), 163–167.
- Cenedese, C., R. E. Todd, G. G. Gawarkiewicz, and W. B. Owens (2013), Offshore transport of shelf waters through interaction of vortices with a shelfbreak current, *J. Phys. Oceanogr.*, 43, 905–919, doi:10.1175/JPO-D-12-0150.1.
- Chapman, D. C., and R. C. Beardsley (1989), On the origin of shelf water in the Middle Atlantic Bight, *J. Phys. Oceanogr.*, 19, 384–391.
- Chen, K., R. He, B. S. Powell, G. G. Gawarkiewicz, A. M. Moore, and H. G. Arango (2014), Data assimilative modeling investigation of Gulf Stream Warm Core Ring interaction with continental shelf and slope circulation, *J. Geophys. Res. Oceans*, 119, 5968–5991, doi:10.1002/2014JC009898.
- Cowen, R. K., J. A. Hare, and M. P. Fahay (1993), Beyond hydrography: Can physical processes explain larval fish assemblages within the Middle Atlantic Bight?, *Bull. Mar. Sci.*, 53(2), 567–587.
- Early, J. J., R. M. Samelson, and D. B. Chelton (2011), The evolution and propagation of quasisynoptic ocean eddies, *J. Phys. Oceanogr.*, 41, 1535–1555, doi:10.1175/2011JPO4601.1.
- Evans, R. H., K. S. Baker, O. B. Brown, and R. C. Smith (1985), Chronology of warm-core ring 82B, *J. Geophys. Res.*, 90(C5), 8803–8811, doi:10.1029/JC090iC05p08803.
- Flierl, G. R., and J. S. Wroblewski (1985), The possible influence of warm core Gulf Stream rings upon shelf water larval fish distribution, *Fish. Bull.*, 83, 313–330.
- Fratantoni, P., R. Pickart, D. Torres, and A. Scotti (2001), Mean structure and dynamics of the shelfbreak jet in the Middle Atlantic Bight during fall and winter, *J. Phys. Oceanogr.*, 31, 2135–2156.
- Gawarkiewicz, G., F. Bahr, R. C. Beardsley, and K. H. Brink (2001), Interaction of a slope eddy with the shelfbreak front in the Middle Atlantic Bight, *J. Phys. Oceanogr.*, 21, 2783–2796.
- Gawarkiewicz, G., K. H. Brink, F. Bahr, R. C. Beardsley, M. Caruso, J. Lynch, and C.-S. Chiu (2004), A large-amplitude meander of the shelfbreak front in the Middle Atlantic Bight: Observations from the Shelfbreak PRIMER Experiment, *J. Geophys. Res.*, 109, C03006, doi:10.1029/2002JC001468.
- Gawarkiewicz, G. G., C. A. Linder, J. F. Lynch, A. E. Newhall, and J. J. Bisagni (1996), A surface-trapped intrusion of slope water onto the continental shelf in the Mid-Atlantic Bight, *Geophys. Res. Lett.*, 23(25), 3763–3766, doi:10.1029/96GL03427.
- Hare, J. A., and R. K. Cowen (1996), Transport mechanisms of larval and pelagic juvenile bluefish (*Pomatomus saltatrix*) from South Atlantic Bight spawning grounds to Middle Atlantic Bight nursery habitats, *Limnol. Oceanogr.*, 41(6), 1264–1280.
- Hare, J. A., J. H. Churchill, R. K. Cowen, T. J. Berger, P. C. Cornillon, P. Dragos, S. M. Glenn, J. J. Govoni, and T. N. Lee (2002), Routes and rates of larval fish transport from the southeast to the northeast United States continental shelf, *Limnol. Oceanogr.*, 47(6), 1774–1789.
- Houghton, R. W., D. Hebert, and M. Prater (2006), Circulation and mixing at the New England shelfbreak front: Results of purposeful tracer experiments, *Progr. Oceanogr.*, 70(2–4), 289–312, doi:10.1016/j.pcean.2006.05.001.

- Kennelly, M. A., R. H. Evans, and T. M. Joyce (1985), Small-scale cyclones on the periphery of the Gulf Stream warm-core ring, *J. Geophys. Res.*, 90(C5), 8845–8857, doi:10.1029/JC090iC05p08845.
- Lee, C. M., and K. H. Brink (2010), Observations of storm-induced mixing and Gulf Stream Ring incursion over the southern flank of Georges Bank: Winter and summer 1997, *J. Geophys. Res.*, 115, C08008, doi:10.1029/2009JC005706.
- Lee, T. N., L. P. Atkinson, and R. Legeckis (1981), Observations of a Gulf Stream frontal eddy on the Georgia continental shelf, April 1977, *Deep-Sea Res.*, 28A(4), 347–378.
- Lentz, S. J. (2003), A climatology of salty intrusions over the continental shelf from Georges Bank to Cape Hatteras, *J. Geophys. Res.*, 108(C10), 3326, doi:10.1029/2003JC001859.
- Lentz, S. J. (2010), The mean along-isobath heat and salt balances over the Middle Atlantic Bight continental shelf, *J. Phys. Oceanogr.*, 40(5), 934–948, doi:10.1175/2009JPO4214.1.
- Linder, C. A., and G. G. Gawarkiewicz (1998), A climatology of the shelfbreak front in the Middle Atlantic Bight, *J. Geophys. Res.*, 103, 18,405–418,423, doi:10.1029/98JC01438.
- Ryan, J. P., J. A. Yoder, and P. C. Cornillon (1999), Enhanced chlorophyll at the shelfbreak of the Mid-Atlantic Bight and Georges Bank during the spring transition, *Limnol. Oceanogr.*, 44(1), 1–11.
- Ryan, J. P., J. A. Yoder, and D. Townsend (2001), Influence of a Gulf Stream warm-core ring on water mass and chlorophyll distributions along the southern flank of Georges Bank, *Deep Sea Res., Part II*, 48(1–3), 159–178.
- Rypina, I. I., J. K. Llopiz, L. J. Pratt, and M. S. Lozier (2014), Dispersal pathways of American eel larvae from the Sargasso Sea, *Limnol. Oceanogr.*, 59(5), 1704–1714, doi:10.4319/lo.2014.59.5.1704.
- Shchepetkin, A. F., and J. C. McWilliams (2008), Computational kernel algorithms for fine-scale, multiprocess, long-term oceanic simulations, in *Handbook of Numerical Analysis. XIV: Computational Methods for the Atmosphere and the Ocean*, edited by P. G. Ciarlet, R. Temam, and J. Tribbia, pp. 121–183, Elsevier Science, Oxford, U. K., doi:10.1016/S1570-8659(08)01202-0.
- Trowbridge, J. H., and S. J. Lentz (1991), Asymmetric behavior of an oceanic boundary layer above a sloping bottom, *J. Phys. Oceanogr.*, 21(8), 1171–1185.
- Wang, Z. A., R. Wanninkhof, W.-J. Cai, R. H. Byrne, X. Hu, T.-H. Peng, and W.-J. Huang (2013), The marine inorganic carbon system along the Gulf of Mexico and Atlantic coasts of the United States: Insights from a transregional coastal carbon study, *Limnol. Oceanogr.*, 58(1), 325–342, doi:10.4319/lo.2013.58.1.0325.
- Warner, J. C., C. R. Sherwood, H. G. Arango, and R. P. Signell (2005), Performance of four turbulence closure models implemented using a generic length scale method, *Ocean Model.*, 8, 81–113.
- Wei, J., and D.-P. Wang (2009), A three-dimensional model study of warm core ring interaction with continental shelf and slope, *Cont. Shelf Res.*, 29, 1635–1642, doi:10.1016/j.csr.2009.05.009.
- Zhang, W. G., and G. G. Gawarkiewicz (2015), Length-scale of the finite-amplitude meanders of shelfbreak fronts, *J. Phys. Oceanogr.*, doi:10.1175/JPO-D-14-0249.1.
- Zhang, W. G., J. L. Wilkin, and O. M. E. Schofield (2010), Simulation of water age and residence time in New York Bight, *J. Phys. Oceanogr.*, 40(5), 965–982.
- Zhang, W. G., D. J. McGillicuddy, and G. G. Gawarkiewicz (2013), Is biological productivity enhanced at the New England Shelfbreak Front?, *J. Geophys. Res. Oceans*, 118, 517–535, doi:10.1002/jgrc.20068.